Optical properties, lattice dynamics, and structural phase transition in hexagonal 2H-BaMnO_{3} single crystals

T. N. Stanislavchuk, A. P. Litvinchuk, Rongwei Hu, Young Hun Jeon, Sung Dae Ji, S.-W. Cheong, and A. A. Sirenko

Phys. Rev. B **92**, 134308 — Published 29 October 2015

DOI: 10.1103/PhysRevB.92.134308

Optical properties, lattice dynamics, and structural phase transition in hexagonal 2H-BaMnO$_3$ single crystals

T. N. Stanislavchuk,[1,a)] A. P. Litvinchuk,[2] Rongwei Hu,[3] Young Hun Jeon,[4,5] Sung Dae Ji,[5] S.-W. Cheong,[3,4,5] and A. A. Sirenko[1]

[1] *Department of Physics, New Jersey Institute of Technology, Newark, New Jersey 07102, USA*

[2] *Texas Center for Superconductivity and Department of Physics, University of Houston, Houston, Texas 77204, USA*

[3] *Rutgers Center for Emergent Materials and Department of Physics and Astronomy, Rutgers University, Piscataway, New Jersey 08854, USA*

[4] *Laboratory for Pohang Emergent Materials, Pohang University of Science and Technology, Pohang 790-784, Korea*

[5] *Max Plank POSTECH Center for Complex Phase Materials, Pohang University of Science and Technology, Pohang 790-784, Korea*

---

a) Author to whom correspondence should be addressed. Electronic mail: stantar@njit.edu.

ABSTRACT

Optical properties and lattice dynamics of hexagonal 2H-$BaMnO_3$ single crystals are studied experimentally in a wide temperature range by means of rotating analyzer ellipsometry and Raman scattering. The magnitude of the direct electronic band gap is found to be E_g = 3.2 eV. At room temperature the far-infrared (IR) ellipsometry spectra reveal six IR-active phonons, two of them are polarized along the *c*-axis and four are polarized within the $a-b$ plane. Seven phonon modes are identified in the Raman scattering experiments. Group theoretical mode analysis and complimentary density functional theory lattice dynamics calculations are consistent with the 2H-$BaMnO_3$ structure belonging to the polar $P6_3mc$ space group at room temperature. All observed vibrational modes are assigned to the specific eigenmodes of the lattice. The neutron diffraction measurements reveal a structural phase transition upon cooling below T_C=130±5 K, which is accompanied by the lattice symmetry change from the $P6_3mc$ to the $P6_3cm$. Simultaneously, at temperatures below T_C several additional IR- and Raman-active modes are detected in experimental spectra. This confirms the occurrence of a structural transition, which is possibly associated with appearance of the electrical polarization along the *c*-axis and a previously known tripling of the primitive cell volume at low temperatures.

PACS number(s): 78.30.-j, 63.20.dh, 75.47.Lx, 75.85.+t

I. INTRODUCTION

The ABO_3 family of crystalline materials is one of the most intensively studied during the last decade. This interest is driven by its known multifunctional properties and its potential for room temperature (RT) multiferroicity, that requires a coexistence of interconnected magnetic and ferroeletric orders in the same compound. In a typical ferroelectric perovskite, like $BaTiO_3$, the ferroelectricity appears due to hybridization of empty 3*d* shells of Ti and occupied 2*p* shells of O.[1] The ferroelectric distortion occurs due to the displacement of *B*-site cation (Ti) with respect to the oxygen octahedra. While this mechanism requires empty 3*d* shells of transition metal, the existence of magnetic order would require at least a partially filled 3*d* shell, thus creating an obstacle on the way to multiferroicity.[2] However this obstacle can be overcome in compounds where different atoms are responsible for ferroelectric and magnetic orders (lone pair mechanism). For example, in a well-studied rhombohedral perovskite $BiFeO_3$ the hybridization of Bi empty 6*p* orbitals and occupied oxygen 2*p* orbitals results in ferroelectric displacement of Bi cation whereas partially occupied 3*d* shells of Fe are responsible for a magnetic order parameter.[3] In hexagonal (h) $RMnO_3$, where *R* stands for rare-earth ions, the structural phase transition results in tilting of MnO_5 bipyramids accompanied by displacements of R^{3+} and oxygen ions which lead to a net ferroelectric polarization, while Mn^{3+} cations establish a magnetic order in the system.[4,5] The mechanism of ferroelectricity in h-$RMnO_3$ is of electrostatic origin rather than due to changes in chemical bonding, like in $BiFeO_3$. Thus, it implies that in properly designed materials the ferroelectricity and magnetism can be driven by the same ion.

One of the systems interesting in this regard is (Ca,Sr,Ba)MnO_3 perovskites. It was shown that Mn spins form a long range antiferromagnetic order with G-type magnetic structure in $CaMnO_3$[6] and $SrMnO_3$[7,8] and triangular arrangement of spins perpendicular to the *c*-axis in $BaMnO_3$[9] (BMO). First principle calculations predict that these compounds possess ferroelectric instability which is Mn-dominated in spite of partial 3*d* state occupancy.[10] This instability is suppressed by antiferrodistortive oxygen motions but it was shown that $CaMnO_3$ can be made ferroelectric by applying an external strain.[11] Thus epitaxial $CaMnO_3$ films with 2.3% tensile strain grown on (001)-oriented $LaAlO_3$ substrates were found to be ferroelectric below 25 K. Since Ba has larger ionic radius compared to Ca, it was suggested that $BaMnO_3$ crystals can possess ferroelectric ground state without external tensile strain but rather due to the chemical pressure.[10,12] The substitution of Ca cations with Ba cations results, however, in a 2H hexagonal structure with face-sharing oxygen octahedra[13] instead of orthorhombic perovskite structure of $CaMnO_3$ with corner-sharing oxygen octahedra.[14] At the same time the exact symmetry of 2H structure and especially the atomic displacements that result in electric polarization are still under debate.

Early experimental optical studies performed by Roy and Budhani[15] on polycrystalline BMO samples revealed 5 Raman modes and 4 infrared (IR) modes. Since in a non-polar centrosymmetric group all Raman modes are different from IR modes due to the exclusion principle, while in a polar group most of the modes are simultaneously IR- and Raman-active, the observed proximity of IR and Raman mode frequencies lead the authors to a conclusion that the RT phase of BMO is polar $P6_3mc$.[15] The structure assignment to this polar group was also supported by recent dielectric measurements of ceramic 2H-BMO samples, where ferroelectric order was observed.[16] At the same time, several x-ray and neutron powder diffraction studies suggest a non-polar $P6_3/mmc$ group at RT.[9,17] Cussen and Battle[9] reported a structural phase transition between RT and 80 K which introduces displacements to MnO_6 chains and results in tripling of the unit cell volume. The authors suggested a polar $P6_3mc$ group for low temperatures (LT) though they didn't rule out the possibility of a centrosymmetric $P\bar{3}c1$ group. Recent first principle calculations performed by Varignon and Ghosez[18] suggest that at room temperature 2H-BMO possesses a stable centrosymmetric $P6_3/mmc$ structure while upon lowering the temperature it should develop an improper ferroelectric structural phase transition into a $P6_3cm$ ground state. The calculations showed that the phase transition is driven mainly by the unstable non-polar K_3 phonon mode, which corresponds to the motion of Mn and O atoms along the *c*-axis. The polarization then arises due to additional condensation of a stable polar Γ_2^- mode triggered by the condensation of the K_3 mode.[18]

Since RT and LT crystal structures are still under debate, we performed neutron powder diffraction measurements and optical studies of 2H-BMO single crystals in order to clarify their ground state and to investigate possible indications of the structural phase transitions. The number of spectroscopically accessible lattice excitations in the crystal is strictly determined by the crystal's symmetry, which makes spectroscopic techniques to be sensitive to crystal's symmetry as well as suitable for detecting phase transitions upon which the symmetry changes. To the best of our knowledge, only unpolarized transmission and Raman measurements on polycrystalline samples have been performed and reported in literature so far. In this paper we present experimental data for the phonon spectra and their polarization analysis measured between 7 K and 300 K. Complimentary density functional lattice dynamics calculations are performed, which allow assignment of the observed vibrational lines to the specific eigenmodes of the structure. Based on the optical phonon data we will present our conclusions about the crystal symmetry of the measured single crystal samples.

II. SAMPLES, EXPERIMENTAL TECHNIQUES, AND LATTICE DYNAMICS CALCULATIONS

2H-BMO single crystals were grown using a flux method at the Rutgers Center for Emergent Materials. BMO crystals have been obtained in the form of translucent flakes with a typical size of $2\times2\times0.15$ mm^3. The size of available BMO crystals allowed only for the ellipsometry measurement from the *a-b* plane. In contrast, the micro-Raman experiments have been performed for the laser light excitation and collection along and perpendicular to the *c*-axis of the crystals. A J.A. Woollam M-2000 spectroscopic ellipsometer at the Center for Functional Nanomaterials at Brookhaven National Lab (CFN-BNL) was used in the spectral range from near-IR up to ultraviolet (UV) at room temperature only. Spectra of the optical phonons were studied in the temperature range between 7 K and 300 K. The far-IR optical experiments were carried out at the National Synchrotron Light Source (NSLS), BNL, at the U4IR beamline equipped with a Bruker 66 interferometer, a custom-made far-IR rotating analyzer ellipsometer (RAE), and a LHe-cooled (4.2 K) bolometer.[19] The spectral resolution in the far-IR experiments was 0.7 cm^{-1}. Raman scattering experiments were performed in the backscattering configuration using 532 nm (Nd:YAG) and 514.5 nm (Ar-ion) laser lines, a LN_2-cooled CCD detector, and single-grating Jobin Yvon spectrometer, which provided a spectral resolution of about 2 cm^{-1}. Neutron powder diffraction data were collected at ST2 HRPD beamline of HANARO Center, Korea using neutron source with λ=1.8344Å.

The first principle lattice dynamics calculations of 2H-$BaMnO_3$ were performed within the generalized gradient approximation using Perdew-Burke-Ernzerhof local functional[20] as implemented in the CASTEP code[21]. Norm-conserving pseudopotentials were used. Prior to performing calculations the structure was relaxed while keeping lattice parameters fixed and equal to the experimentally determined ones (a=0.56991 nm, c=0.48145 nm) for the space group P*6₃mc*, so that forces on atoms in the equilibrium position did not exceed 20 meV/nm. The integration within the Brillouin zone was performed over 5×5×6 Monkhorst-Pack grid in the reciprocal space. Lattice dynamics was further assessed by tre;ating a 3×3×2 supercell by final displacement method, which yields frequencies of transverse optical (TO) modes.

III. EXPERMENTAL RESULTS AND DISCUSSION

A. Neutron diffraction measurements

In order to determine the crystal structure of 2H-BMO crystals we performed temperature dependent neutron powder diffraction measurements in the range from 5 K to 300 K [see Fig.1(a)]. The samples for powder diffraction with the mass of about 5 g were obtained from the same growth run as the larger size flakes that were used for optical studies. At room temperature the crystal structure was equally well refined with the centrosymmetric $P6_3/mmc$ and polar $P6_3mc$ symmetry groups (see Fig. 2). With lowering the temperature to T_C=130 K 2H-BMO undergoes structural phase transition upon which the tripling of unit cell occurs and crystal symmetry group lowers from $P6_3mc$ ($P6_3/mmc$) to $P6_3cm$ in agreement with Cussen and Battle.[9] Figure 2(a) shows a number of structural peaks that appear in the diffraction spectra for $T< T_C$. The correspondence between the unit cell parameters of high (a',c') and low ($a_0\,,c_0$) temperature phases is as follows: $a' \approx \sqrt{3}a_0$, $c' \approx c_0$ and in vector form $\vec{a}' = 2\vec{a}_0 + \vec{b}_0$, $\vec{b}' = -\vec{a}_0 + \vec{b}_0$, $\vec{c}' = \vec{c}_0$

. Figure 1(b) shows temperature dependence of the a and c unit cell parameters obtained from the crystal structure refinement. The error bars for the a and c parameters are comparable with size of the symbols in Fig. 1(b). In order to keep the *a*-parameter continuity across the phase transition we define as follows: $a = a'$, $c = c'$ for low temperature phase and $a = \sqrt{3}a_0$, $c = c_0$ for high temperature phase. While temperature behavior of the a parameter doesn't show any peculiarity and monotonically decreases with lowering the temperature, the c parameter manifests a kink at T_C=130 K and starts increasing below the transition temperature. The fact that the lattice expands along *c* below T_C may be related to the coupling between ferroelectric polarization, which appears in polar $P6_3cm$ symmetry below T_C and is directed along the *c*-axis, and uniform strain along the *c*-axis. Such a coupling could indicate that polarization *P* and Curie temperature T_C can be controlled by the strain along the *c*-axis. More detailed analysis of neutron diffraction data (structural and magnetic peaks) and related dielectric studies will be published elsewhere.

While neutron diffraction measurements enabled us to determine the LT symmetry of 2H-BMO crystal ($P6_3cm$ space group) it could not distinguish between $P6_3/mmc$ and $P6_3mc$ symmetry groups for the RT phase. As we will discuss in the next sections, symmetry based selection rules for optical phonons in crystals possessing centrosymmetric $P6_3/mmc$ and polar $P6_3mc$ space groups are different, thus giving us a possibility to distinguish between those two groups.

B. Optical properties measured by spectroscopic ellipsometry

In this section we will present spectroscopic ellipsometry data for 2H-BMO, which will be also compared with that for hexagonal *R*MnO$_3$ (*R* = rare earth) crystals. Ellipsometry measurements were carried out in the spectral range between 0.75 eV and 5.9 eV. Figures 3(a) and 3(b) show experimental spectra for the real $\langle \varepsilon_1(\omega) \rangle$ and imaginary parts of the pseudo dielectric function $\langle \varepsilon(\omega) \rangle$ and measured at the multiple angles of the light incidence (AOI) between 55° and 75°. Due to hexagonal symmetry, the dielectric function tensor is diagonal in the Cartesian *x,y,z* coordinate system (*c*||*z*) with $\varepsilon_{xx}(\omega)=\varepsilon_{yy}(\omega)=\varepsilon_{\perp}(\omega)$ and $\varepsilon_{zz}(\omega)=\varepsilon_{\parallel}(\omega)$. In the measured configuration, when the reflection plane of the sample coincided with the $a-b$ crystallographic plane, $\left\langle\varepsilon\left(\omega\right)\right\rangle$ is a function of AOI = ϕ and the tensor components $\varepsilon_{\perp}(\omega)$, $\varepsilon_{\parallel}(\omega)$ at each frequency ω:[22,23]

$$\langle\varepsilon\rangle=\sin^2(\phi)\cdot\left[1+\sin^2(\phi)\left\{\frac{\varepsilon_{\perp}\sqrt{\varepsilon_{\perp}-\sin^2(\phi)}-\sqrt{\dfrac{\varepsilon_{\perp}\left[\varepsilon_{\parallel}-\sin^2(\phi)\right]}{\varepsilon_{\parallel}}}}{\varepsilon_{\perp}\cos^2(\phi)-\sqrt{\varepsilon_{\perp}-\sin^2(\phi)}\cdot\sqrt{\dfrac{\varepsilon_{\perp}\left[\varepsilon_{\parallel}-\sin^2(\phi)\right]}{\varepsilon_{\parallel}}}}\right\}^2\right]\tag{1}$$

The observed weak angular dependence of the measured ellipsometry spectra did not allow us to decouple the in-plane and out-of-plane components of the complex dielectric function: $\varepsilon_{\perp}(\omega)$ and $\varepsilon_{\parallel}(\omega)$. At the same time, Eq.(1) shows that the main contribution to $\left\langle\varepsilon(\omega)\right\rangle$ comes from $\varepsilon_{\perp}(\omega)$, while contribution from $\varepsilon_{\parallel}(\omega)$ is significant only near zeros of the real part of $\varepsilon_{\parallel}(\omega)$ function. In the measured spectral range, however, it is very unlikely that $\varepsilon_1(\omega)$ could achieve zero value (see for example Fig. 3(a), where $\left\langle\varepsilon_1(\omega)\right\rangle$ is above 2 in all spectral range). Thus, the contribution from $\varepsilon_{\parallel}(\omega)$ should be small and for modeling of $\left\langle\varepsilon_{1,2}(\omega)\right\rangle$ spectra we can consider the $\varepsilon_{\parallel}(\omega)$ to be constant, for example equal to 3.6 that is low frequency value of measured $\left\langle\varepsilon_1(\omega)\right\rangle$ function, without any significant influence on the modeling result. The experimental spectra in Figs. 3(a) and 3(b) are dominated by a few strong absorption peaks above 3 eV. Electronic structure calculations performed for orthorhombic[24] and hexagonal[25] manganites along with photo emission and X-ray absorption data[26,27] show that closest to the Fermi level are Mn(3*d*) and O(2*p*) states. The strong peaks above 3 eV were observed in both ortho- and hexa- manganites and attributed to allowed O(2*p*) – Mn(3*d*) charge transfer (CT) transitions.[24,28,29,30] The contribution of these CT transitions to the in-plane dielectric response was modeled with three isotropic Lorentz oscillators and a Penn gap oscillator:

$$\varepsilon_{\perp}(\omega) \approx \langle \varepsilon(\omega) \rangle = 1 + \sum_{k=1}^{4} \frac{S_k \cdot E_{k,0}{}^2}{E_{k,0}{}^2 - \omega^2 - i\gamma_k \omega}, \qquad (2)$$

where $E_{k,0}$ is the electronic transition energy, S_k is the oscillator strength for the interband optical transition, and γ_k represents the broadening. Three Lorentz oscillators (k=1,2,3) at 3.2 eV, 3.9 eV, and 5.1 eV belong to the spectral range covered in our experiments. The lowest direct band gap at E_g = 3.2 eV is at the high energy edge of the visible spectral range and its value does not contradict the translucent appearance of the measured BMO single crystals. The Penn gap (k=4) at 8.6 eV is above the high-energy limit of our measurements and, thus, may not correspond to any real electronic transitions. This Penn gap has been included in the dielectric function model to take into account all other higher-energy optical transitions above 6 eV and to match the experimental low-energy value of $\langle \varepsilon_1(\omega) \rangle$, which is about 3.6. The parameters of the Penn gap and the Lorentz oscillators for the electronic transitions in BMO crystals are summarized in Table I and the fit results are shown in Figs. 3(a) and 3(b) with red curves.

While the origin of the strong CT electronic transitions is quite clear, this is not the case for a weak peak marked with an asterisk and positioned at 2.5 eV. Note that electronic transition peaks in the range of 1 eV to 3 eV were observed in both ortho- and hexa- manganites, but their structure and intensity differs substantially between these systems that is attributed to different environment of Mn^{3+} ions, different crystal field (CF) splitting of Mn 3*d* manifold and different level of hybridization between O(2*p*) and Mn(3*d*) orbitals in ortho- and hexa- manganites. Figure 3(c) shows experimental ellipsometry data of $\langle \varepsilon_2(\omega) \rangle$ for a *hexagonal* single crystal RMnO$_3$ with *R*=Lu measured also from the *a-b* plane. Unlike the case of 2H-BMO, spectrum of LuMnO$_3$ is dominated by an intense and narrow band at about 1.6 eV. This peak, which is predominantly excited by the electric field of light $\vec{E} \perp c$, has been also observed in other hexagonal RMnO$_3$ (*R*-rare-earth or yttrium).[25,29,30,31,32] There are still debates in literature regarding the nature of this transition. The CF of D_{3h} symmetry inside trigonal MnO$_5$ bipyramids splits Mn^{3+} *d* orbitals into 3 groups: e'' (xz, yz), e' (xy, x^2-y^2) and a_1' (3z^2-r^2) in order of energy increase[25]. According to

Hund's rule, four 3*d* electrons of Mn^{3+} ion occupy e'' and e' orbitals to form high spin state while the a_1' orbital is empty. One interpretation of the 1.6 eV peak is that it corresponds to the onsite *d*-*d* transition between Mn^{3+} orbitals which are hybridized with oxygen orbitals.[30,31] Another interpretation is that 1.6 eV peak is related to a transition from high energy O(2*p*) states to Mn(da_1') state.[26,29,33] Finally it was suggested that, because of strongly hybridized nature of the occupied states, the peak at 1.6 eV should be related to transition from O(2*p*) orbitals, which are hybridized with Mn 3*d* orbitals of the same symmetry, to unoccupied Mn a_1' orbital, rather than to strictly *d*-*d* or *p*-*d* transition.[25,34]

The 1.6 eV peak is known to be absent in the spectra of orthorhombic RMnO$_3$ manganites,[24,35] which possess a weaker peak at ~2 eV with a fine structure.[24,28,36] We note that the structure of this peak in ortho-RMnO$_3$ is retained for different R^{3+} ions[24] while in h-RMnO$_3$ the position of ~1.6 eV peak shifts by ~0.1 eV with the change of R^{3+} ion.[25,32] In contrast to h-RMnO$_3$ with trigonal MnO$_5$ bipyramids, orthorhombic manganites, as well as 2H-BMO, are composed of MnO$_6$ octahedrons. The *d* orbitals of Mn^{3+} ion in ortho-RMnO$_3$ are split by O_h octahedral CF into two groups: t_{2g} (xz, yz, xy) and e_g (3z^2-r^2,x^2-y^2) which are further split by Jahn-Teller (JT) distortion[37]. Four 3*d* electrons of Mn^{3+} ion occupy three t_{2g} orbitals and the lower e_g orbital to form high spin state while upper e_g orbital is empty. Theoretical studies showed that the observed weak peak at 2 eV originates from intersite nearest neighbor de_g-de_g CT transition[24,38] while its weak structure corresponds to O($t_{2u}(\pi)$) - Mn(e_g) and parity forbidden but phonon assisted O($t_{1g}(\pi)$) - Mn(e_g) CT transitions.[24] In contrast to $3d^4$ electronic configuration of Mn^{3+} ions in ortho-RMnO$_3$, the electronic configuration of Mn^{4+} ions in 2H-BMO is $3d^3$, just like in CaMnO$_3$. The latter crystal is composed of the same MnO$_6$ octahedrons as ortho-RMnO$_3$, but due to $3d^3$ electronic configuration of Mn^{4+} ions their e_g orbitals are unoccupied. Thus, the intersite de_g-de_g transition at ~2 eV typical for ortho-RMnO$_3$ was not observed in CaMnO$_3$ which appeared to be transparent below 3 eV.[39] While both 2H-BMO and CaMnO$_3$ are composed of MnO$_6$ octahedra with Mn^{4+} ions, the symmetries of Mn cites are different in these compounds. In $P6_3mc$ structure of 2H-BMO Mn^{4+} ions occupy positions with C_{3v} symmetry inside face sharing MnO$_6$ trigonal antiprisms which form chains along the *c*-axis, while in *Pbnm* structure of $CaMnO_3$ Mn^{4+} ions occupy positions with O_h symmetry inside corner sharing MnO_6 octahedra. Lowering of symmetry from O_h to C_{3v} splits one-electron t_{2g} orbitals into a_1 singlet and e doublet; e_g doublet remains unsplit but because of the absence of inversion symmetry it becomes e level[40]. According to Hund's rule, three d^3 electrons of Mn^{4+} ion occupy a_1 and lower e orbitals to form high spin state while upper e orbitals are empty. Since MnO_6 octahedra in 2H-BMO do not share oxygen ions in the *a-b* plane, like in ortho-$RMnO_3$, we can rule out the possibility of intersite nearest neighbor *d-d* CT transition in Mn^{4+} ions as excited by $\vec{E} \perp c$ (*a-b* plane CT transition). The dipole allowed on-site d-d transitions for the $\vec{E} \perp c$ polarization are from a_1 and lower e orbitals to upper e orbitals. Thus, we assume, that the weak peak observed at 2.5 eV and marked with an asterisk in Figs. 3(a) and 3(b) is either due to on-site Mn^{4+} $a_1, e \rightarrow e$ transitions or due to charge transfer transitions from high energy O(2*p*) states to Mn(3d) states. To clarify the nature of the observed weak peak further electronic band structure calculations along with temperature dependent spectroscopic measurements are needed.

C. Far-IR ellipsometry measurements of optical phonons

Spectra of the IR-active optical phonons in BMO single crystals have been measured with spectroscopic RAE from the *a-b* reflection plane of the sample using a single value for AOI=75°. Taking into account that RT crystal symmetry is described by one of the *P6₃/mmc* or *P6₃mc* space groups, the following phonon modes are optically accessible: modes with E_1 symmetry as electric dipoles polarized in *a-b* plane and modes with A_1 symmetry as electric dipoles polarized along the *c*-axis. Figures 4(a) and 4(b) show experimental data for the real and imaginary parts of the pseudo dielectric function, $\langle \varepsilon_1(\omega) \rangle$ and $\langle \varepsilon_2(\omega) \rangle$. The optical spectra were fitted with an anisotropic model function

$$\begin{aligned} \varepsilon_{\parallel}(\omega) &= \varepsilon_{\infty,\parallel} + \sum_{n=1}^{N} \frac{S_{n,\parallel} \cdot \omega_{n,\parallel}^{2}}{\omega_{n,\parallel}^{2} - \omega^2 - i\gamma_{n,\parallel}\omega}, \\ \varepsilon_{\perp}(\omega) &= \varepsilon_{\infty,\perp} + \sum_{m=1}^{M} \frac{S_{m,\perp} \cdot \omega_{m,\perp}^{2}}{\omega_{m,\perp}^{2} - \omega^2 - i\gamma_{m,\perp}\omega}, \end{aligned} \tag{3}$$

consisting of M Lorentz oscillators polarized in the *a*-*b* plane (E_1 modes) and N oscillators polarized along the *c*-axis (A_1 modes). For RT experiments, M =4 and $N=2$, while at LT the number of phonon modes polarized in the *a*-*b* plane increases to M=5. In Eqs. (3) $\omega_{m(n),\parallel(\perp)}$ is the phonon frequency, $S_{m(n),\parallel(\perp)}$ is the phonon oscillator strength, $\gamma_{m(n),\parallel(\perp)}$ stands for the phonon broadening, and $\varepsilon_{\infty,\parallel(\perp)}$ represents the dielectric constant at frequencies above those of the measured optical phonons but below the near IR spectral region discussed in the previous section ($\varepsilon_1(0.75\text{ eV}) \approx 3.6$). The results of the fit using Eqs. (3) are shown in Figs. 4(a) and 4(b) with red curves. All modes polarized in the *a*-*b* plane are marked as AB_m (m=1,2,3,4) while those polarized along the *c*-axis are marked as C_n (n=1,2). The phonon mode which appears at LT and polarized in the *a*-*b* plane is marked with an asterisk. We note, that in ellipsometric spectra obtained from *a*-*b* reflectance plane of the sample, phonon modes polarized in the *a*-*b* plane manifest themselves at transverse optical (TO) frequencies, while those polarized along the *c*-axis appear at their longitudinal optical (LO) frequencies, or where $\varepsilon_{\parallel}(\omega) = 0$. In Fig. 4 the positions of AB_m and C_n labels correspond to TO frequencies of the phonon modes. For this reason the positions of C_n labels are at the low frequency side from the spectral lines corresponding to the C_n modes. Also, spectra in Fig. 4 show two spectral features at ~230cm^{-1} and ~700cm^{-1} at which the pseudo dielectric function $\langle \varepsilon_2 \rangle$ becomes negative. These features appear at LO frequencies of phonon modes polarized in the *a*-*b* plane and are reasonably fitted with our model without introducing any additional oscillators. We note that while true dielectric function ε_2 is always positive, pseudo dielectric function $\langle \varepsilon_2 \rangle$ in anisotropic materials, as shown in Eq.(1), could become negative that doesn't contradict any physics laws. The parameters of the optical phonons are summarized in Table II. The experimental value of $\varepsilon_{\infty,\parallel}$ is determined to be 2.9. This experimental value is in a reasonable agreement with the low-energy value of $\varepsilon_1(0.75\text{ eV}) = 3.6$ from the optical data presented in the previous section.

Due to the small size of the BMO crystals available to us, the low-frequency range of the spectra in Figs. 4(a) and 4(b) is affected by both the diffraction limit and diffused light scattering by the edges of the small samples. These effects revealed themselves in an artificial decrease of the pseudo-dielectric function $\langle \varepsilon_1(\omega) \rangle$ for low frequencies and an increase of $\langle \varepsilon_2(\omega) \rangle$ in the spectral range below ~150 cm^{-1}, where the wavelength of light becomes comparable with the apparent size of the measured sample at AOI=75°. Note that this artifact of the measurements practically does not influence the obtained values of the phonon frequencies. The quasi-static value of $\varepsilon_{1,\perp}(0)$ is found as a sum of $\varepsilon_{\infty,\perp}$ and the combined oscillator strength of all four optical phonons $\varepsilon_{1,\perp}(0) = \varepsilon_{1,\perp,\infty} + \sum_{m=1}^{M} S_m$. The uncertainty in the experimental values of the low-frequency phonon oscillator strength results in the correspondingly high uncertainty of the quasi-static value of $\varepsilon_{1,\perp}(0) = 9 \pm 3$.

D. Raman scattering experiments

Spectra of the optical phonons in the same crystals of 2H-BMO have been also studied using Raman scattering. Several back-scattering configurations were utilized: $c(a,a)\overline{c}$, $a(c,c)\overline{a}$, $a(b,b)\overline{a}$, and $a(c,b)\overline{a}$, where the first and the last symbols correspond to the *k*-vector direction for exciting and scattered light, whereas symbols in brackets correspond to the polarization direction of the excitation and scattering light waves. In these geometries the following mode symmetries should become accessible[41]: A_1+E_2, A_1, A_1+E_2, and E_1, as in-plane x- and y-axes could not be distinguished for a hexagonal crystal. As shown in Fig. 5, experimental spectra are not completely polarized. Several A_1 symmetry modes could, however, be reliably identified in the $a(c,c)\overline{a}$ spectrum (at 368 and 492 cm^{-1}), while relatively high intensity of the 120 and 530 cm^{-1} modes in the $c(a,a)\overline{c}$ spectrum proves them as being of E_2 symmetry. It is worth noting that the modes at 639 and 660 cm^{-1} observed in Raman spectra are very close in frequency with those detected in IR spectra (639 and 653 cm^{-1}) and being assigned to the A_1 and E_1 symmetry, respectively. A relatively week and broad feature observed in the spectra around 590 cm^{-1} and marked with an asterisk in Fig. 5 could probably be attributed to the phonon second order scattering processes. The experimentally observed phonon frequencies and their symmetries are summarized in

Table II along with the results of first principle calculations for the space group *P6₃mc*. It seems that there is a reasonable agreement between experimental and calculated mode frequencies.

The behavior of phonon modes in IR and Raman spectra can be better understood if we consider corresponding atomic displacements, some of which are shown in Fig. 6. The fully symmetric A_1 mode corresponds to the symmetric breathing of oxygen atoms around Mn, and its strong Raman intensity (see the 644 cm^{-1} mode in Fig. 5) can be attributed to a large polarizability of the mode. However, its infrared intensity is not high (see C_2 mode in Figs. 4 and 7) due to only a small dipole moment generated along the *c*-axis via a slightly out-of the *a-b*-plane vibration of oxygen. For a similar reason, the non-polar E_2 mode also has a large Raman intensity (see the 530 cm^{-1} mode in Fig. 5). The E_1 mode, which involves contribution from the in-plane oxygen and Mn displacements, is, instead, rather strong in the infrared spectrum (see AB_4 mode in Figs. 4 and 7.).

E. Temperature dependence of the phonon frequencies

Temperature dependence of the IR optical phonon frequencies is shown in Fig. 7. The oxygen motion-related high frequency modes (AB_3, AB_4 and C_2) along with the low-frequency mode AB_1 demonstrate a natural softening with the temperature increase. This common behavior is known to be caused by the thermal expansion of the lattice and anharmonic phonon–phonon interactions, which become more important as the temperature increases due to the statistical increase of the number of phonons. We fitted the temperature dependence of the $AB_{1,3,4}$ and C_2 phonons using the following equation:[42]

$$\omega_0(T) = \omega_{0|T=0} \times \exp\left[-3\gamma_G \int_0^T \alpha(T')dT' \right], \tag{4}$$

where γ_G is a Grüneisen parameter, $\alpha(T)$ is the linear expansion coefficient along the corresponding *a*- or *c*-axis, and $\omega_{0|T=0}$ is the phonon frequency at zero temperature. $\alpha(T)$ was obtained as derivative of the temperature dependencies of a and c lattice parameters shown in Fig. 1(b). The results of the calculation are shown in Fig. 7 with red curves. Typical values of the Grüneisen parameters for the modes polarized in the *a-b* plane are found to be $\gamma_G = 1.1 \pm 0.1$.

The low-frequency mode AB_2 shows a weak, *e.g*., non-Grüneisen, hardening with the temperature increase. The oscillator strengths of the IR modes, which are also shown in Fig. 7, are nearly temperature independent. This observation predicts the absence of a phonon-driven variation of the quasi-static dielectric constant $\varepsilon_{\perp}(0,T)$ with temperature. Below the structural transition temperature T_C = 130 K we observed an appearance of a weak mode at 641 cm^{-1} which is labeled with an asterisk in Fig. 7. Appearance of the new phonon mode at LT indicates on the transition to a structure with a lower symmetry.

Our ellipsometry data for the *c*-axis polarized phonons C_1 and C_2 are not as clear as that for the *a-b* plane modes. The mode position was identified, but the experimental data for their oscillator strength are less accurate. Much larger crystals with at least a few mm along the *c*-axis would be required for more accurate studies. Temperature dependence of the two *c*-axis polarized phonons C_1 and C_2 is shown in Fig.7. The high-frequency mode at 639 cm^{-1} demonstrates a Grüneisen-like behavior with $\gamma_G = 1.5$ close to that for the *a-b* plane modes. Thus, at room temperature we observed 6 strong IR-active phonons, 4 of which are polarized in the *a-b* plane and 2 are polarized along the *c*-axis. In the low-temp phase $T< T_C$ additional weak phonon polarized in the *a-b* plane appears at ~641cm^{-1}.

Temperature dependence of the Raman-active phonons is shown in Fig. 8. The most remarkable observation is the appearance of the A_1 mode at 368 cm^{-1} for $T< T_C$ [see Figs. 8(a) and 8(b)]. This phonon appears only in the $a(c,c)\overline{a}$ configuration that corresponds to its polarization along the *c*-axis. The normalized amplitude of this mode has a strong step-like behavior typical for the first-order phase transitions at T =130 K. For $T< T_C$ two other higher frequency modes at 417 cm^{-1} and 492 cm^{-1} split into doublets of nearly equal intensity peaks with the splitting of ~2 cm^{-1} [see Figs. 8 (c-f)]. The high-frequency A_1 mode at 660 cm^{-1} has a non-Grüneisen temperature dependence at low temperatures with a kink at $T = T_C$ [see Fig. 8(d)]. This behavior of the A_1 phonons, splitting and softening below T_C, indicates a possible appearance of electrical polarization in the non-centrosymmetric LT phase below 130 K.

To conclude this Section, we repeat that at room temperature we observed 7 Raman-active modes. For $T < T_C$ one extra mode appeared with polarization along the *c*-axis and two phonons split into doublets. The total number of observed Raman modes in the LT phase increases to 10.

F. Crystal symmetry discussion

Presented here experimental data provide important information for analysis of the 2H-$BaMnO_3$ structure. First, we have to mention the number and symmetries of expected vibrational modes for several relevant structures. $P6_3/mmc$ and $P6_3mc$ space groups (Z=2) have 10 atoms per unit cell, which generate 30 degrees of freedom. For the centrosymmetric space group $P6_3/mmc$ one expects $2A_{2u}+3E_{1u}$ (IR), $A_{1g}+E_{1g}+3E_{2g}$ (Raman), $A_{2u}+E_{1u}$ (acoustic) and $A_{2g}+2B_{1g}+B_{1u}+2B_{2u}+2E_{2u}$ (silent) modes, while for the space group $P6_3mc$ group theory predicts $3A_1+4E_1$ (IR), $3A_1+4E_1+5E_2$ (Raman), A_1+E_1 (acoustic) and $A_2+4B_1+B_2$ (silent) modes. Note that according to group theory for non-centrosymmetric $P6_3mc$ group all IR modes are allowed to be observed in Raman spectra, while for centrosymmetric $P6_3/mmc$ group all IR modes are different from Raman modes. The number of observed IR and Raman modes at room temperature (6 IR modes and 7 Raman modes) is higher than the number of modes expected for the $P6_3/mmc$ space group (5 IR modes and 5 Raman modes), a fact which allows us to exclude this space group from the possible candidates for the RT phase. For the same reason the space group $P6_3cm$ (Z=6) can be excluded as well, for which a much larger number of modes is expected due to tripling of the unit cell volume: $8A_1+14E_1$ (IR) as well as $8A_1+14E_1+15E_2$ (Raman). Thus, our experimental findings point toward the $P6_3mc$ space group as being the most appropriate for room temperature structure of 2H-$BaMnO_3$. A critical point here is that experimentally several modes (A_1 at 639/639 cm^{-1} and E_1 mode at 653/660 cm^{-1}), as measured in the IR and Raman spectra, practically coincide in frequency, a fact, that indicates absence of inversion symmetry for the structure.

IV. CONCLUSION

The electronic structure of 2H-$BaMnO_3$ is found to be different from a related family of hexagonal *R*MnO_3 manganites (where *R*=Y, Ho, Er, Tm, Yb, Lu) by the absence of the strong "red band" at about 1.6 eV, which is typical for latter compounds. Instead, a weak peak was observed at 2.5 eV, which we assume corresponds to transition from Mn a_1 or lower e orbitals to Mn upper e orbitals or from high energy O(2*p*) states to Mn(3*d*) states. The fundamental direct optical gap is found to be at E_g = 3.2 eV. The neutron diffraction measurements for 2H-BMO single crystal reveal the existence of a structural transition from $P6_3mc$ ($P6_3/mmc$) symmetry at room temperature to $P6_3cm$ for temperature below T_C=130 K. While temperature behavior of lattice parameter a doesn't show any peculiarity, the c parameter manifests a kink at T_C=130 K and starts increasing below the transition temperature, which may be related to the coupling between ferroelectric polarization and uniform strain along the *c*-axis in the polar LT $P6_3cm$ phase. The far-IR ellipsometry spectra reveal 6 IR-active phonons at room temperature, (two of them are polarized along the *c*-axis and four are polarized within the $a-b$ plane), while Raman scattering experiments show seven vibrational modes. Group-theory mode analysis and complimentary density functional theory lattice dynamics calculations are consistent with the 2H-$BaMnO_3$ belonging to polar space group $P6_3mc$ rather than centrosymmetric $P6_3/mmc$ at room temperature. All observed vibrational modes are assigned to the specific eigenmodes of the lattice. Below T_C=130 K of the structural phase transition, new modes in IR and Raman spectra have been observed. An appearance of a new mode, splitting of several existing Raman modes, and softening of the high-frequency mode for $T< T_C$ are consistent with the tripling of the primitive cell in the low-temperature phase and possible appearance of polarization at the LT phase.

ACKNOWLEDGMENTS

The authors are thankful to Ken Ahn at NJIT and Yuri Janssen and Peter Khalifah at SUNY Stony Brook for useful discussions and to Y. J. and P. Kh. for help with X-ray measurements at RT. The ellipsometry and Raman scattering measurements and crystal growth at NJIT and Rutgers were supported by DOE DE-

FG02-07ER46382. Lattice dynamics calculations and low-temperature Raman scattering experiments were carried out by A.P.L. who acknowledges the support of the State of Texas through the Texas Center for Superconductivity at the University of Houston. Use of the National Synchrotron Light Source, Brookhaven National Laboratory, was supported by DOE DE-AC02-98CH10886. Near-IR-VIS ellipsometry measurements at the Center for Functional Nanomaterials, Brookhaven National Laboratory, have been supported by DOE DE-AC02-98CH10886. The neutron diffraction measurements of the lattice parameters at Postech were supported by the Max Planck POSTECH/KOREA Research Initiative Program [Grant No. 2011-0031558] through NRF of Korea funded by MSIP.

TABLE I. Experimental parameters of the strong Lorentz oscillators that have been used to model the spectral dependence of the $\langle \varepsilon_1 \rangle$ and $\langle \varepsilon_2 \rangle$ shown in Figs. 3(a) and 3(b). The oscillator strength S_k is in units of $\langle \varepsilon_1 \rangle$.

	E_k, eV	γ_k, eV	S_k
Oscillator 1	3.2	0.5	0.3(5)
Oscillator 2	3.9	1.0	1.2(5)
Oscillator 3	5.1	1.6	1.0
Penn gap	8.6	1.3	0.1

ε_1(0.75 eV)=3.6

TABLE II. Frequencies and symmetries of the experimental IR- and Raman-active phonons at RT in comparison with DFT-calculated values for the $P6_3mc$ space group. All phonon frequencies are in cm^{-1}. (2) means a doublet at LT. * is for LT modes.

Phonon symmetry	IR (exper.)	Raman (exper.)	DFT calc.
A_1	82		64
E_2		119	128
E_1	145		119
E_2		344	324
A_1		368*	
E_1	394		385
E_2			393
E_2		413(2)	436
A_1		487 (2)	468
E_2		526	518
E_1	599		486
A_1	639	639	684
E_1	641*		
E_1	653	660	611

$\varepsilon_{\perp,\infty} = 2.9$

FIGURES

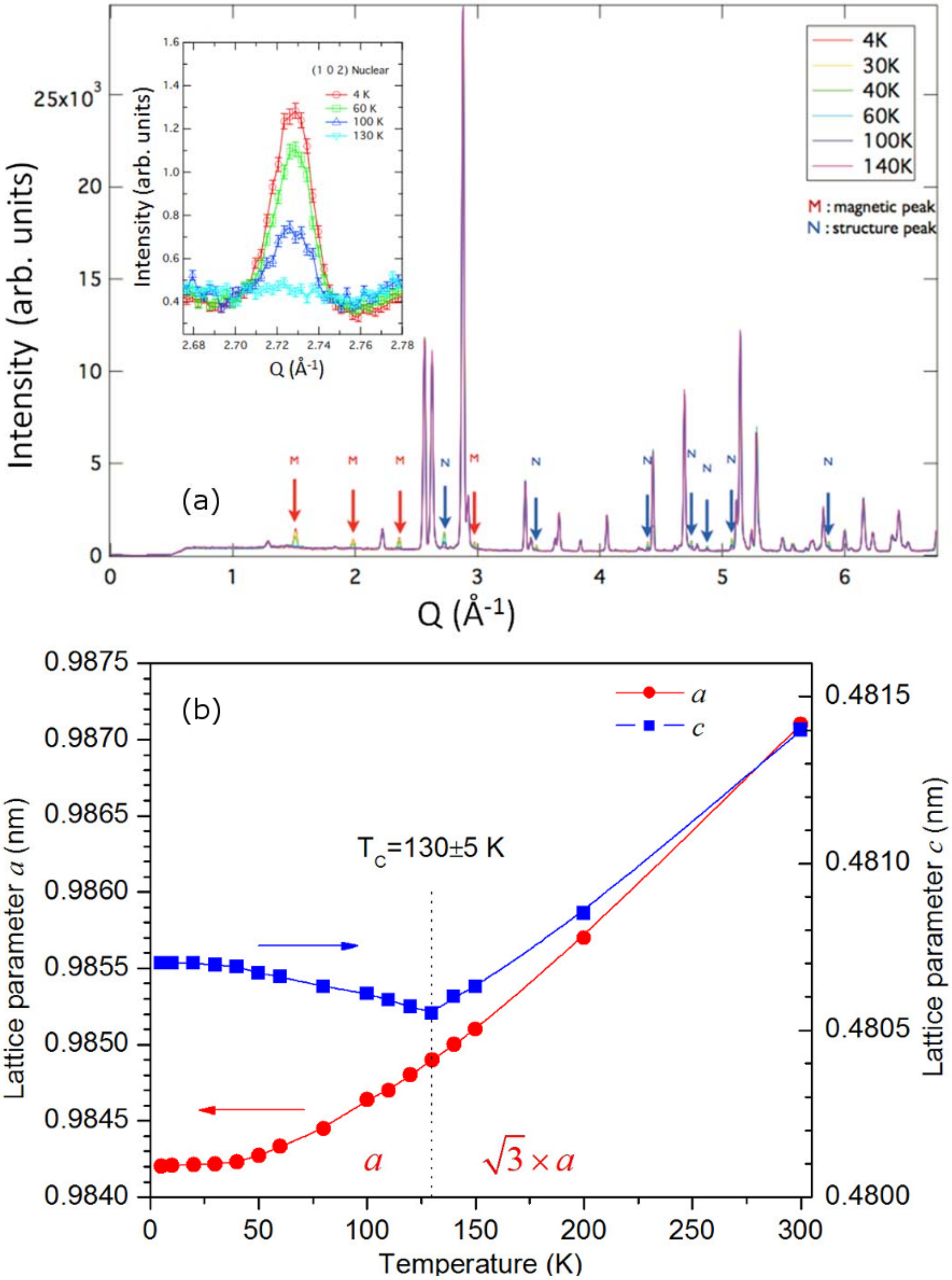

FIG. 1. (Color online) (a) Neutron diffraction data measured at several temperatures below (T = 4 K, 30 K, 40 K, 60 K, 100 K) and above (T=140 K) the structural transition. Symbols M and N mark the magnetic and structural peaks. The inset shows temperature variation for one of the structural peaks that disappears in the high-temperature phase above T_C =130±5 K. (b) Neutron diffraction data for the temperature dependence of the 2H-BMO lattice parameters.

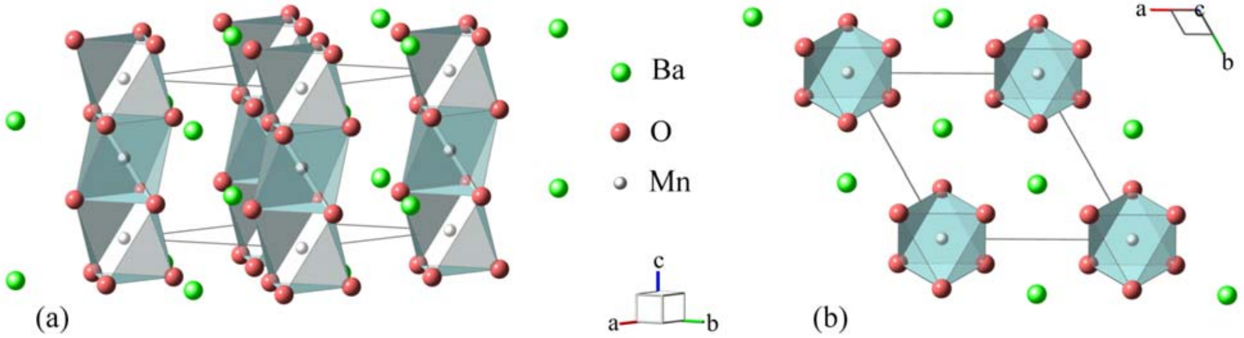

FIG. 2. (Color online) Crystallographic structure of 2H-BMO featuring face-sharing MnO_6 octahedrons (space group $P6_3mc$) from (a) side view and (b) top view.

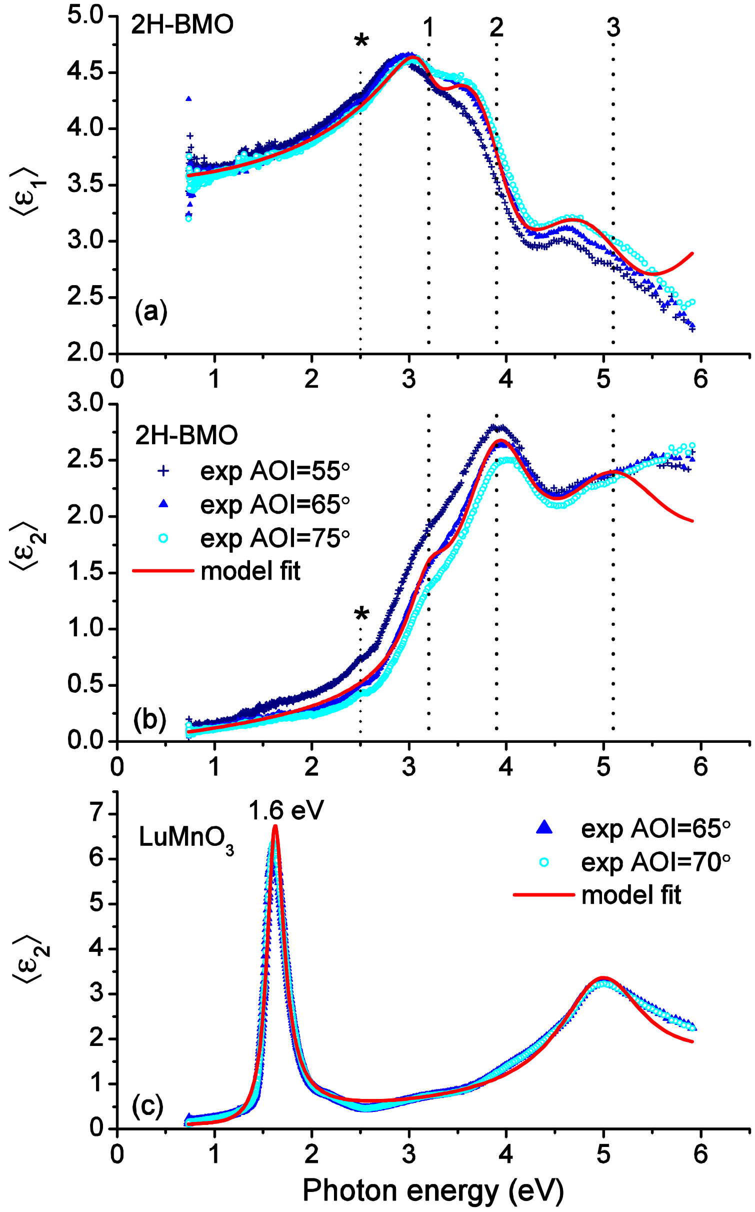

FIG. 3. (Color online) (a) The real $\langle \varepsilon_1(\omega) \rangle$ and (b) imaginary $\langle \varepsilon_2(\omega) \rangle$ parts of the pseudo dielectric function (symbols) for a BMO single crystal measured at room temperature from the *a-b* plane with three values of AOI: 55, 65, and 75 deg. The results of the fit using dielectric function model that consists of three oscillators and a Penn gap (see Table I) are shown with red solid curves. (c) Experimental data for $\langle \varepsilon_2(\omega) \rangle$ in h-LuMnO$_3$. Note a strong absorption peak at 1.6 eV that is absent in (b).

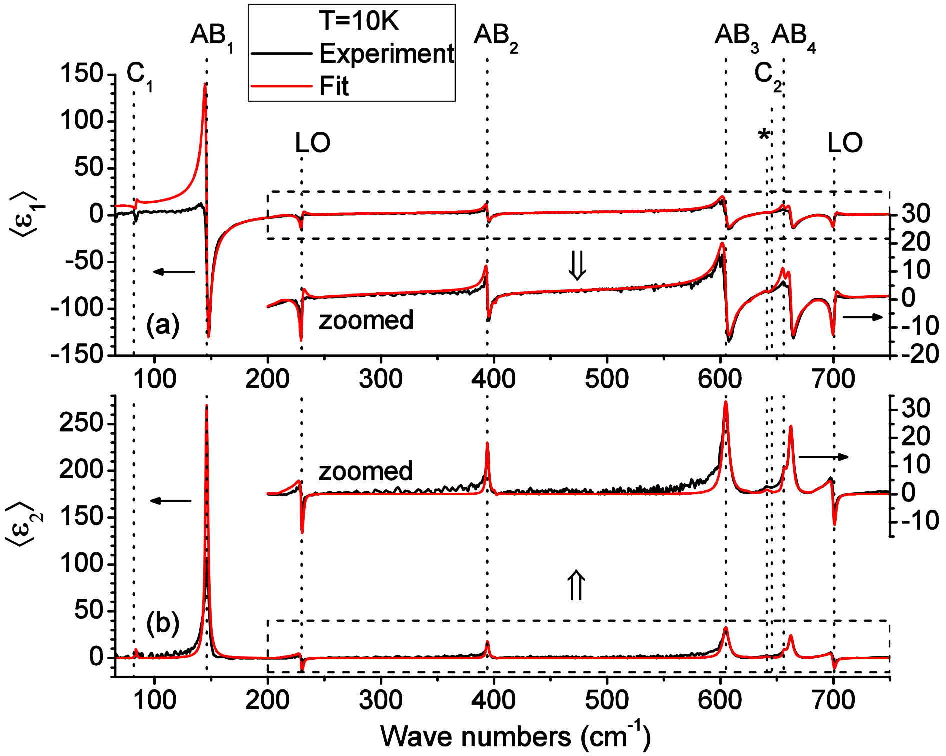

FIG. 4. (Color online) (a) The real and (b) imaginary parts of the measured pseudo dielectric function $\langle \varepsilon_1(\omega) \rangle$ and $\langle \varepsilon_2(\omega) \rangle$ (black curves) for a BMO single crystal measured for T=10 K from the *a*-*b* plane with AOI=75 deg. The results of the fit using dielectric function model that consists of 7 oscillators are shown with red solid curves. The AB_m and C_n labels mark TO frequencies of the phonon modes. For this reason the positions of C_n labels are at the low frequency side from the spectral lines corresponding to C_n modes since they manifest themselves at LO frequencies in the current configuration of the measurements.

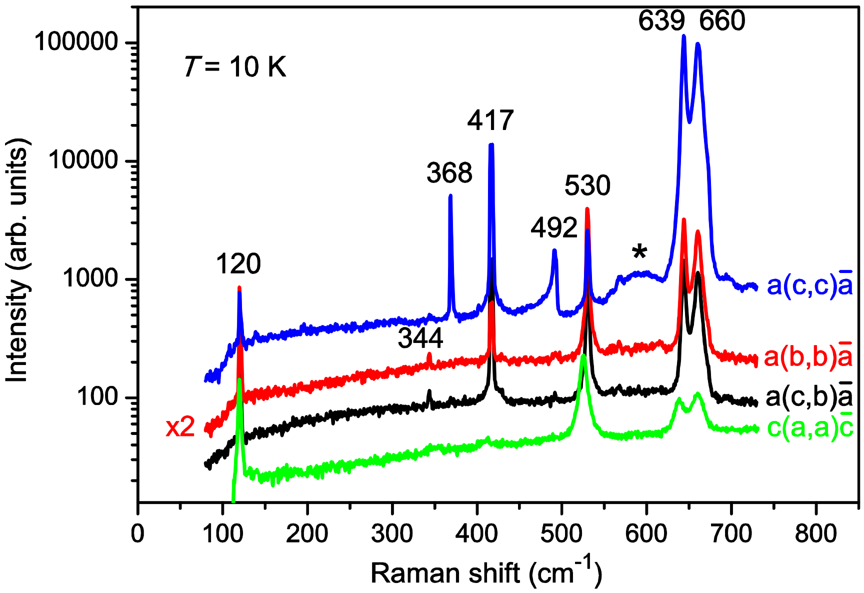

FIG. 5. (Color online) Low-temperature Raman spectra measured in four complementary scattering geometries: $c(a,a)\overline{c}$, $a(c,c)\overline{a}$, $a(b,b)\overline{a}$, and $a(c,b)\overline{a}$. The phonon peaks are marked according to their frequencies.

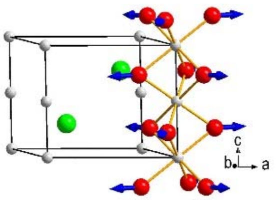

A_1 - 684 cm^{-1}

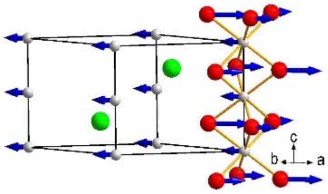

E_1 - 611 cm^{-1}

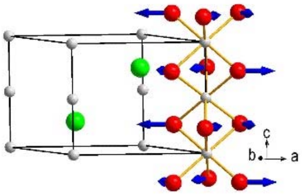

E_2 - 518 cm^{-1}

FIG. 6. (Color online) DFT-calculated atomic displacements corresponding to several high frequency phonon modes.

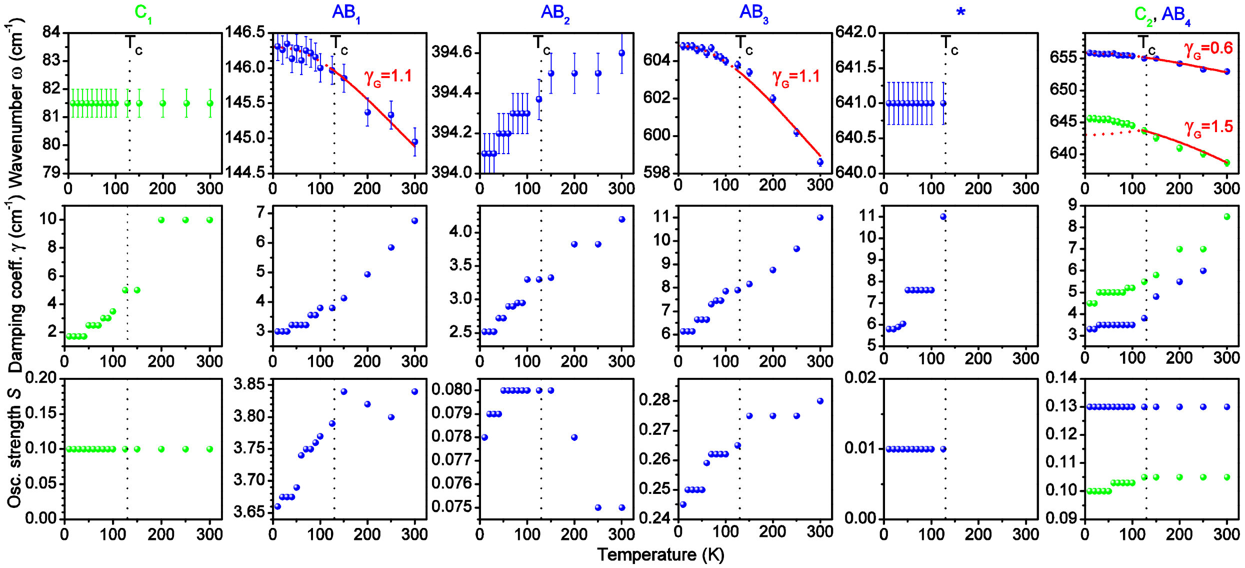

FIG. 7. (Color online) Temperature dependencies for parameters of the IR-active optical phonons. The red curves on graphs for lines AB_1, AB_3, AB_4 and C_2 are fits using Eq. (3) with the Grüneisen parameter γ_G shown next to the curves. The structural transition temperature of T_C = 130 K is shown with the vertical dashed line.

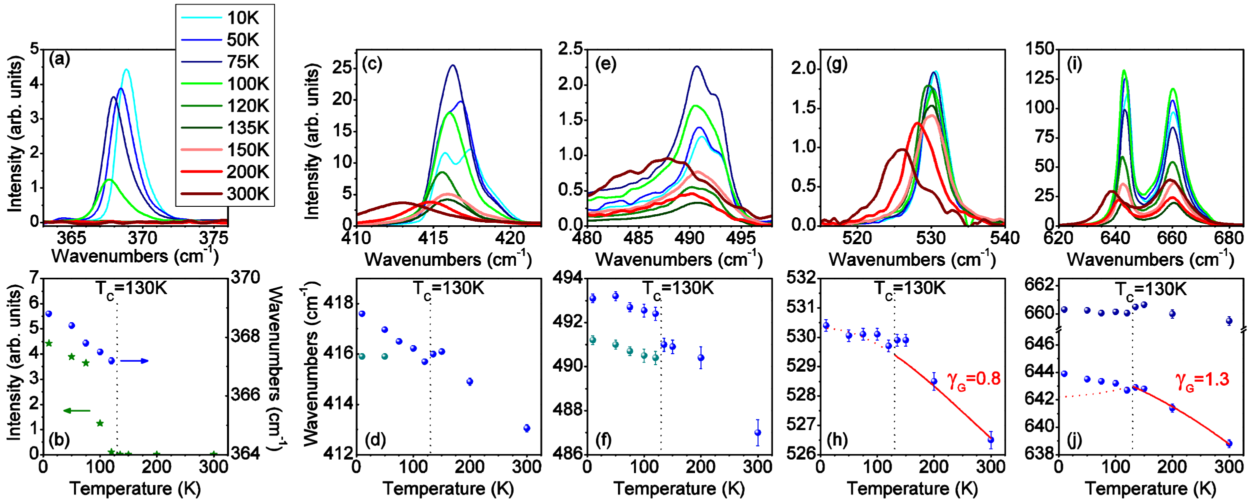

FIG. 8. (Color online) Temperature dependence of the Raman-active phonons measured in the $a(c,c)\bar{a}$ configuration. (a,b) Appearance of a new mode at 369 cm^{-1} for $T < T_C$. (c-f) Splitting of the phonons at 417 cm^{-1} at 492 cm^{-1}. (g-h) Grüneisen-like hardening of the phonon at 530 cm^{-1} with $\gamma_G = 0.8$. (i-j) Phonon at 660 cm^{-1} with a kink at $T = T_C$ and Grüneisen hardening of the phonon at 644 cm^{-1} with $\gamma_G = 1.3$.

REFERENCES

---

[1] R. E. Cohen, Nature **358**, 136 (1992).

[2] N. A. Hill, J. Phys. Chem. B **104**, 6694 (2000).

[3] J. B. Neaton, C. Ederer, U. V. Waghmare, N. A. Spaldin, and K. M. Rabe, Phys. Rev. B **71**, 014113 (2005).

[4] B. B. Van Aken, T. T. M. Palstra, A. Filippetti, and N. A. Spaldin, Nature Mater. **3**, 164 (2004).

[5] Craig J. Fennie and Karin M. Rabe, Phys. Rev. B **72**, 100103R (2005).

[6] E. O. Wollan and W. C. Koehler, Phys. Rev. **100**, 545 (1955).

[7] P. D. Battle, T. C. Gibb, and C. W. Jones, J. Solid State Chem. **74**, 60 (1988).

[8] A. Daoud-Aladine, C. Martin, L. C. Chapon, M. Hervieu, K. S. Knight, M. Brunelli, and P. G. Radaelli, Phys. Rev. B **75**, 104417 (2007).

[9] E. J. Cussen and P. D. Battle, Chem. Mater. **12**, 831 (2000).

[10] Satadeep Bhattacharjee, Eric Bousquet, and Philippe Ghosez, Phys. Rev. Lett. **102**, 117602 (2009).

[11] T. Günter, E. Bousquet, A. David, Ph. Boullay, Ph. Ghosez, W. Prellier, and M. Fiebig, Phys. Rev. B **85**, 214120 (2012).

[12] James M. Rondinelli, Aaron S. Eidelson, and Nicola A. Spaldin, Phys. Rev. B **79**, 205119 (2009).

[13] B. L. Chamberland, A. W. Sleight, and J. F. Weiher, J. Solid State Chem. **1**, 506 (1970).

[14] K. R. Poeppelmeier, M. E. Leonowicz, J. C. Scanlon, and J. M. Longo, J. Solid State Chem. **45**, 71 (1982).

[15] Chaintali Roy and R. C. Budhani, Phys. Rev. B **58**, 8174 (1998).

[16] S. Satapathy, M. K. Singh, Pragya Pandit, and P. K. Gupta, Appl. Phys. Lett. **100**, 042904 (2012).

---

[17] A.N. Christensen and G. Ollivier, J. Solid State Chem. **4**, 131 (1972).

[18] Julien Varignon and Philippe Ghosez, Phys. Rev. B **87**, 140403(R) (2013).

[19] T. N. Stanislavchuk, T. D. Kang, P. D. Rogers, E. C. Standard, R. Basistyy, A. M. Kotelyanskii, G. Nita, T. Zhou, G. L. Carr, M. Kotelyanskii, and A. A. Sirenko, Rev. Sci. Instr. **84**, 023901 (2013).

[20] John P. Perdew, Kieron Burke, and Matthias Ernzerhof, Phys. Rev. Lett. **77**, 3865 (1996).

[21] S.J. Clark, M.D. Segall, C.J. Pickard, P.J. Hasnip, M.J. Probert, K.Z. Refson, and M.C. Payne, Z. Kristallogr. **220**, 567 (2005).

[22] R. Basistyy, T. N. Stanislavchuk, A. A. Sirenko, A. P. Litvinchuk, M. Kotelyanskii, G. L. Carr, N. Lee, X. Wang, and S.-W. Cheong, Phys. Rev. B **90**, 024307 (2014).

[23] G. E. Jellison, Jr. and J. S. Baba, J. Opt. Soc. Am. A **23**, 468 (2006).

[24] A. S. Moskvin, A. A. Makhnev, L. V. Nomerovannaya, N. N. Loshkareva, and A. M. Balbashov, Phys. Rev. B **82**, 035106 (2010).

[25] Woo Seok Choi, Dong Geun Kim, Sung Seok A. Seo, Soon Jae Moon, Daesu Lee, Jung Hyuk Lee, Ho Sik Lee, Deok-Yong Cho, Yun Sang Lee, Pattukkannu Murugavel, Jaejun Yu, and Tae W. Noh, Phys. Rev. B **77**, 045137 (2008).

[26] J.-S. Kang, S. W. Han, J.-G. Park, S. C. Wi, S. S. Lee, G. Kim, H. J. Song, H. J. Shin, W. Jo, and B. I. Min, Phys. Rev. B **71**, 092405 (2005).

[27] K. Asokan, C.L. Dong, C.W. Bao, H.M. Tsai, J.W. Chiou, C.L. Chang, W.F. Pong, P. Duran, C. Moure, O. Pena, Solid State Commun. **134**, 821 (2005).

[28] N. N. Kovaleva, A.V. Boris, C. Bernhard, A. Kulakov, A. Pimenov, A.M. Balbashov, G. Khaliullin, and B. Keimer, Phys. Rev. Lett. **93**, 147204 (2004).

[29] A. M. Kalashnikova and R. V. Pisarev, JETP Lett. **78**, 143 (2003).

---

[30] A.B. Souchkov, J.R. Simpson, M. Quijada, H. Ishibashi, N. Hur, J.S. Ahn, S.W. Cheong, A.J. Millis, and H.D. Drew, Phys. Rev. Lett. **91**, 027203 (2003).

[31] R. C. Rai, J. Cao, J. L. Musfeldt, S. B. Kim, S.-W. Cheong, and X. Wei, Phys. Rev. B **75**, 184414 (2007).

[32] A. A. Makhnev and L. V. Nomerovannaya, Physics of Metals and Metallography **114**, 910 (2013).

[33] J. E. Medvedeva, V. I. Anisimov, M. A. Korotin, O. N. Mryasov, and A. J. Freeman, J. Phys.: Condens. Matter **12**, 4947 (2000).

[34] A. S. Moskvin and R. V. Pisarev, Low Temperature Physics **36**, 489 (2010).

[35] Woo-Chul Yi, Sook-Il Kwun and Jong-Gul Yoon, J. Phys. Soc. Jap. **69**, 2706 (2000).

[36] M. A. Quijada, J. R. Simpson, L. Vasiliu-Doloc, J. W. Lynn, H. D. Drew, Y. M. Mukovskii, and S. G. Karabashev, Phys. Rev. B **64**, 224426 (2001).

[37] J. A. Alonso, M. J. Martínez-Lope, M. T. Casais, M. T. Fernández-Díaz, Inorg. Chem. **39**, 917 (2000).

[38] K. H. Ahn and A. J. Millis, Phys. Rev. B **61**, 13545 (2000).

[39] J. H. Jung, K. H. Kim, D. J. Eom, T. W. Noh, E. J. Choi, Jaejun Yu, Y. S. Kwon, Y. Chung, Phys. Rev. B **55**, 15489 (1997).

[40] F. A. Cotton, *Chemical applications of group theory* (Wiley, New York, 1990).

[41] R. Loudon, Adv. Phys. **13**, 423 (1964).

[42] J. Ménéndez and M. Cardona, Phys. Rev. B **29**, 2051 (1984).